

Article

Investigation on Disaster Mechanism of Diversion Tunnel Induced by Gripper TBM in Hydrokarst Erosion Stratum and Engineering Measures

Tengtian Yang ^{1,2} 

¹ China Railway Construction Bridge Engineering Bureau Group Co., Ltd., Tianjin 300300, China; 15596883707@163.com

² Shaanxi Key Laboratory of Geotechnical and Underground Space Engineering, Xi'an 710055, China

Abstract: In gripper tunnel boring machine (TBM) tunneling through complex geological formations, the safe and efficient recovery from large-scale collapses remains a formidable challenge. In this study, we investigate the causes of a 1246 m³ collapse that occurred during the gripper TBM tunneling in the diversion tunnel in Xinjiang, China. Various techniques including TSP seismic waves, CFC advanced water exploration, laboratory point load tests and packer permeability tests were employed for thorough research. The examination discloses that the water softening in biotite-quartz schist in fractured zones contributes significantly to the loosening and dislocation of rock layers along joints. The gripper TBM's cutterhead exacerbates this process through cutting action and vibrations, causing large-scale instability and eventual rock mass collapse. To tackle this engineering problem, we propose a three-step treatment scheme comprising "Reinforcement-Backfill-Re-excavation". Furthermore, we propose a technique to handle TBM collapses by creating a "protective shell" within the cavity. The safety and feasibility of these proposed solutions were thoroughly validated through numerical simulations. Also, we utilized the Hoek-Brown theory and Rostami prediction formula to establish recommended values for the total thrust and total torque of the TBM during the collapsed section. The proposed treatment scheme and estimated parameters were successfully applied, resulting in a comprehensive solution from collapse handling to tunneling. This study offers valuable details on effectively managing large-scale collapses in gripper TBM tunneling, which can be useful for similar tunnel engineering and improve safety and efficiency.

Keywords: diversion tunnel; gripper TBM; unfavorable geology; collapse cavity; measures



Citation: Yang, T. Investigation on Disaster Mechanism of Diversion Tunnel Induced by Gripper TBM in Hydrokarst Erosion Stratum and Engineering Measures. *Buildings* **2024**, *14*, 625. <https://doi.org/10.3390/buildings14030625>

Academic Editors: Eugeniusz Koda, Hongming He and Yongjiao Wu

Received: 11 December 2023

Revised: 24 January 2024

Accepted: 21 February 2024

Published: 27 February 2024



Copyright: © 2024 by the author. Licensee MDPI, Basel, Switzerland. This article is an open access article distributed under the terms and conditions of the Creative Commons Attribution (CC BY) license (<https://creativecommons.org/licenses/by/4.0/>).

1. Introduction

In recent years, the tunnel boring machine (TBM) has been widely used in tunnel construction for its advantages of excavation speed, engineering quality, tunneling safety, low carbon emission, and economic benefits, and has become the primary construction method for long railway tunnels and water diversion tunnels [1–3]. However, in unfavorable geology such as high ground stress, squeezing rocks, and fault-fracture zones, TBM encounters significant challenges, making it easy for destructive accidents like water-gushing, mud inflowing, collapses, and shield jamming [4–6]. These incidents not only lead to project delays and economic losses but also jeopardize tunneling safety [7,8]. For instance, Iran's Zagros water conveyance tunnel experienced an 8-month shutdown due to incidents of jamming and collapses caused by fault zones with water-bearing gouges and squeezing formations [9]. China's Qinling Diversion Tunnel encountered 159 instances of rock bursts attributed to the high-stress surrounding rock [10]. Similarly, Turkey's Water Diversion Tunnel faced 18 occurrences of TBM jamming due to squeezing formations, which took 192 days to resolve [11]. Moreover, Japan's S Diversion Tunnel encountered TBM jamming in the presence of high ground stress, eventually leading to construction abandonment [12].

The majority of TBM tunnel accidents, such as collapses and jamming, occur near fault-fractured zones, accounting for up to 54% of incidents [13]. The rock mass in these fault-fractured zones is relatively loose, and the disturbance generated during tunnel construction alters the original stability of the surrounding rock, leading to potential collapses in the tunnel roof and face [14]. Moreover, tunneling disturbances in water-rich fault zones may result in catastrophic water inflows or mud inflows, causing TBM breakdown and support system failure [15]. Nowadays, when a tunnel collapses, the only way to remove the frictional resistance caused by the fallen rocks on the TBM shield is through manual excavation to prevent the TBM jamming. Working in collapsed cavities can be extremely dangerous, especially in unfavorable geology [16–18]. Therefore, it is essential to investigate the reasons behind tunnel collapses completely. This helps pinpoint the instability mechanisms of the TBM tunnel and provides a basis for accurately repairing the collapsed cavity and planning re-excavation processes with science and accuracy.

This paper presents a case study of a large-scale collapse in a diversion tunnel in the Xinjiang Uygur Autonomous Region, China. The investigation aims to pinpoint the causes of substantial collapses during the gripper TBM's traversal through unfavorable geology. Diverse technical methods, such as TSP seismic wave detection, CFC advanced groundwater exploration, laboratory load testing, and packer permeability tests, were utilized to unveil the reasons behind the extensive collapses. Based on the investigation results, a rapid and flexible TBM collapse management technique was proposed, and the feasibility of the proposed scheme was verified by finite element analysis (FEA). The parameters for TBM re-excavation are estimated using the Hoek-Brown theory and the Rostami prediction formula. Ultimately, the restoration scheme was successfully implemented for the collapsed cavity of the diversion tunnel, yielding favorable results. The proposed approach can offer valuable insights for tackling similar engineering challenges in the future.

2. Tunnel Geological Environment and Collapse Situation

2.1. Overview of the Diversion Tunnel

The diversion tunnel project is located in the Altay Prefecture of Xinjiang Uygur Autonomous Region of China, with a total length of 26.718 km and a starting and ending mileage of K2 + 370 m~K29 + 187 m. The satellite image of the diversion tunnel project is shown in Figure 1. The ground elevation is higher towards the east and north and lower towards the west and south, with a longitudinal tunnel slope at 1/3000. The area has low mountains and hills with elevations ranging from 730 to 1400 m, resulting in a difference of 670 m in relative height. The diversion tunnel, linked to the Burqin River through an artificial channel, extends from northwest to southeast. It employs a gripper tunnel boring machine (TBM), commonly called an open-type tunnel boring machine (TBM) in China [19], as the primary excavation method.

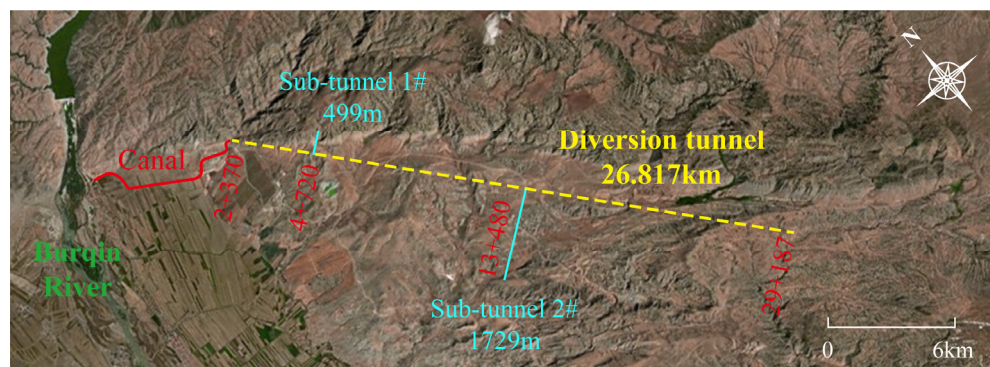


Figure 1. Satellite image of diversion tunnel project.

The construction section is 23.737 km, with an excavation diameter of 7.80 m and a finished tunnel diameter of 7 m. It should be noted that the gripper TBM employs supporting

structures to stabilize the tunnel wall, withstanding the reaction forces and torque during forward advancement. This type of TBM is well-suited for hard-rock tunnels primarily characterized by rock masses of class II and III [20]. It can also be used for soft rock tunnels with effective support measures. The surrounding rock of the diversion tunnel displays geological characteristics indicative of water-rock dissolution. Along the excavation route, gullies are observed, with a maximum burial depth of 668 m, highlighting the significant influence of erosional processes. To adapt to the complex geological environment, the gripper TBM is equipped with advanced drilling and grouting equipment, steel arch installation devices, shotcrete equipment, and various other auxiliary tools.

2.2. Geotechnical Conditions of the Study Area

Figure 2 illustrates the geological profile of the collapsed section in diversion tunnel. The bedrock that the diversion tunnel traverses within the interval from station K4 + 740 to K7 + 932 m is primarily composed of Ordovician biotite quartz schist with varying degrees of weathering, metamorphic granite, exhibiting light gray and dark gray colors. The TBM-excavated section is characterized by moderately developed faults and undulating fracture surfaces, with distinct occurrences of sericite alteration. Mineral composition analysis indicates a quartz content exceeding 50% in the rock. Geological investigations reveal that the weak weathered layer of the bedrock is 8–12 m thick, while the strongly weathered layer measures 3–5 m in thickness. The bedding orientation of the rock layers ranges from 295 to 300 degrees NE azimuth, dipping at an angle of 50 to 60 degrees. The inclination angle for the tunnel axis ranges from 15 to 20 degrees. The tunnel is situated at depths ranging from 23 to 668 m, and along the tunnel alignment, there are 13 secondary small-scale faults. The width of the fault crushed zones generally ranges from 0.50 to 2.50 m, with a maximum width of 8–10 m. Within these crushed zones, cataclastic and fragmented rock materials predominate. At a point where the TBM reached station K6 + 843 m, a large-scale collapse occurred in the diversion tunnel. The tunnel's depth at this location was 8 m, and the volume of the collapse reached 1246 m³.

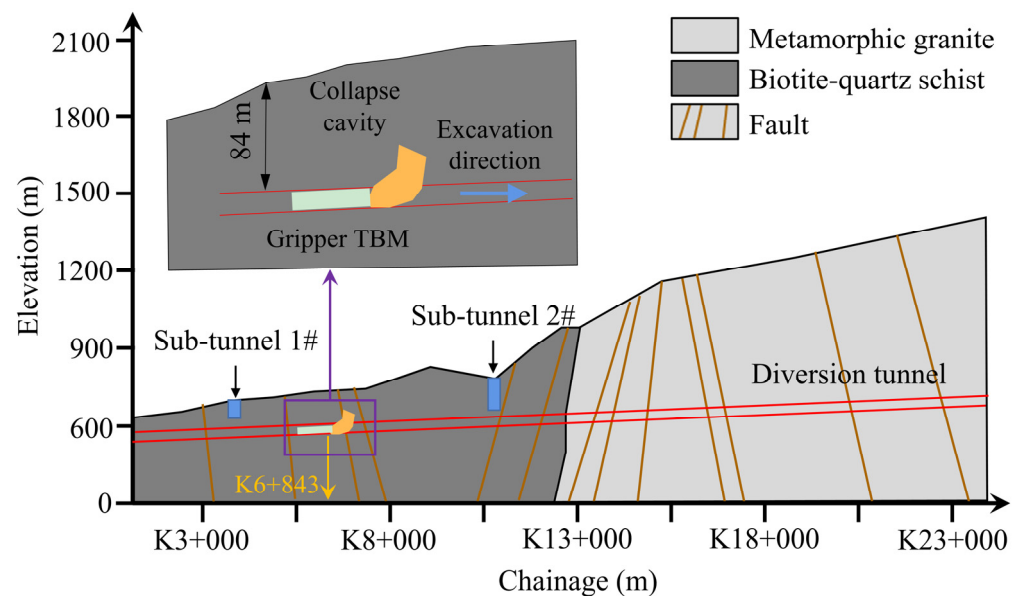


Figure 2. Geological profile of diversion tunnel with collapse cavity location.

2.3. Collapse Disaster of the TBM Tunnel Face

During the TBM excavation, a crack extending from the top of the TBM shield to the tunnel face was encountered, eventually leading to a large-scale collapse. The specific evolution process is as follows. On 12 July 2018, at 10:40 a.m., a significant crack extending towards the tunnel face was observed at the top of the shield when the TBM advanced to

mileage K6 + 837.00. The surrounding rock exhibited significant fragmentation, accompanied by rock falls, as shown in Figure 3a. Reinforcement support was applied using steel bar arrangements, and the type of steel arch support was changed from HW125 to HW150, as shown in Figure 3b. On 12 July 2018, at 11:05 p.m., the thrust force increased to 6230 kN and the monitoring system issued an abnormal debris warning when the TBM advanced to mileage K6 + 840.70. Upon inspection, numerous large pieces of rock debris were identified, accompanied by the observation of a crack in the rock extending along the shield toward the tunnel face. However, no collapse was witnessed in the shield's top direction.

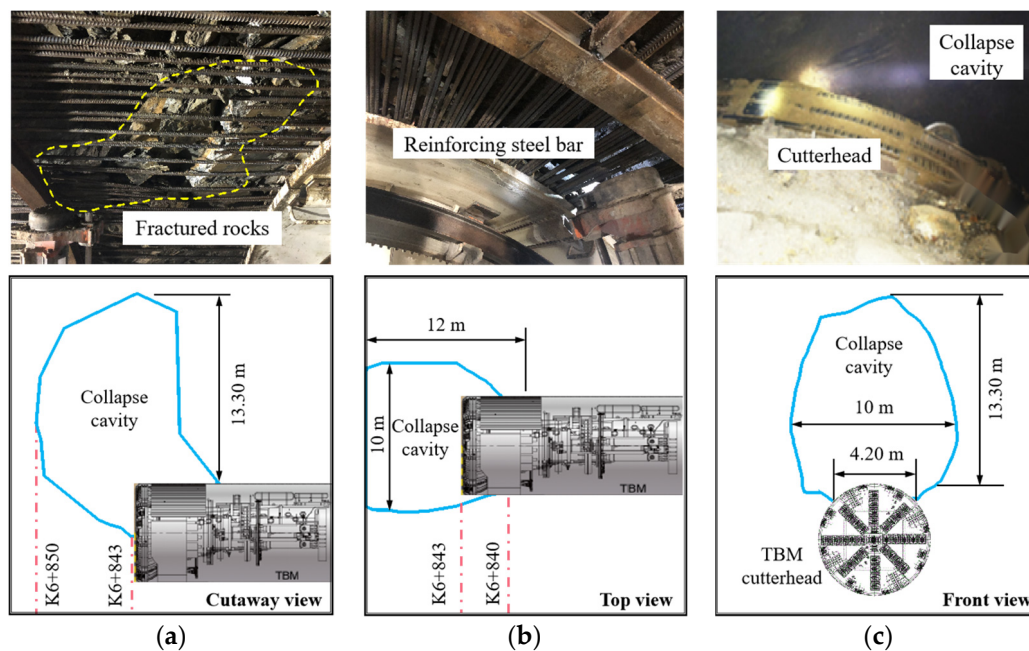


Figure 3. Photos of tunnel collapse progression: (a) dropping fractured rocks; (b) strengthened support with reinforcing steel bar; and (c) collapse situation.

In addition, on 13 July 2018, at 4:30 a.m., a cavity was observed above the TBM shield at the 10–2 o'clock direction when the TBM advanced to mileage K6 + 842.30. The cavity height at the tail of the shield was 0.70 m, extending towards the tunnel face, with a longitudinal length of about 9 m and a height of collapse at the tunnel face of about 8 m, accompanied by falling rock fragments. To prevent further rock fragment collapses, the affected area was immediately reinforced with shotcrete. After completing this tunneling cycle, the support category for the surrounding rock was upgraded from Class III to Class IV to provide better support. On 13 July 2018, at 11:26 a.m., the collapse of the roof rock intensified and the TBM excavation was immediately stopped to reinforce the arch when the TBM advanced to mileage K6 + 843.00. The cutterhead was rotating normally, but the TBM's excavation-induced disturbance caused continuous rock spalling. Ultimately, a large-scale collapse of approximately 1246 m³ occurred, with the approximate dimensions of length, width, and height of 12 m, 10 m, and 13.30 m, respectively. The final shape and dimensions of the collapse cavity are depicted in Figure 3.

3. Analysis of the Disaster Mechanism of Tunnel Collapse

3.1. Advance Geology Forecast

In examining the causes of extensive collapses during gripper TBM traversals through fractured zones, tunnel seismic prediction (TSP) and complex frequency conductivity (CFC) exploration techniques were utilized to scrutinize the characteristics of the surrounding rock, see Appendix A for technical details.

After encountering a collapse at the K6 + 843 m section during TBM excavation, TSP seismic wave detection [21] was conducted ahead of the tunnel face, yielding the geological

structure displacement image within the range of K6 + 843 m to K6 + 923 m, as depicted in Figure 4a. The amplitude of reflection corresponds to the reflection coefficient, where red denotes positive reflection coefficients, and blue signifies negative reflection coefficients. The presence of a combination of red and blue indicates the inferior stability and integrity of the surrounding rock, suggesting a more fragmented rock mass [22]. It can be inferred that the surrounding rock between K6 + 843 m and K6 + 875 m exhibits joint fractures or fold development, indicative of fragmented and low-strength rock. The section from K6 + 843 m to K6 + 855 m constitutes the collapse zone, with the surrounding rock relatively intact within the excavation range from K6 + 855 m to K6 + 865 m. However, the rock mass outside the left wall of the tunnel exhibits low strength and poor integrity. The rock mass between K6 + 889 m to K6 + 901 m and K6 + 918 m to K6 + 923 m features well-developed joint fractures and primarily consists of weak interlayers, displaying fragmented and low-strength characteristics.

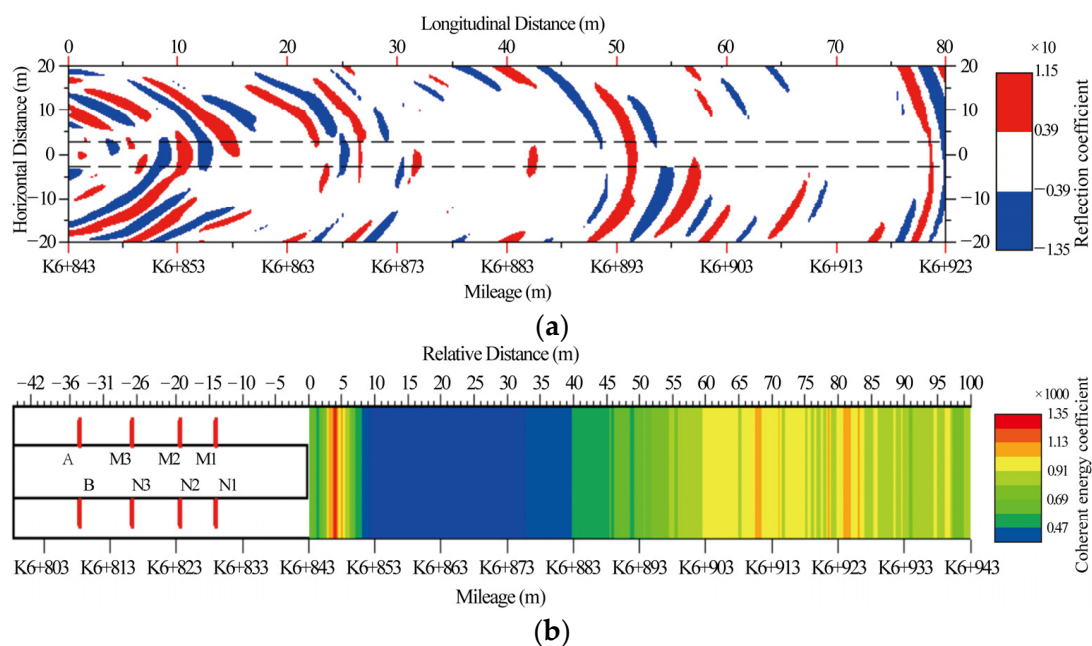


Figure 4. Results of advance geology forecast: (a) TSP seismic migration image (b) CFC migration image.

Furthermore, conducting CFC advanced groundwater exploration ahead of the tunnel face provided insight into underground water distribution within the range of K6 + 843 m to K6 + 943 m, as presented in Figure 4b. The transition in the image representation from warm tones to cool tones signifies a gradual decrease in coherent energy, indicating a shift from high to low relative moisture content in the surrounding rock. As coherent energy strengthens, reflective waves intensify, reflecting a higher moisture content and increased water saturation [23]. According to the exploration result, the average dielectric constant of the surrounding rock within the range of K6 + 843 m to K6 + 943 m is 2.841. Combining the image, it is evident that there is a significant disparity in water content. However, in the interval from K6 + 843 m to K6 + 851 m, there is an extremely strong coherence energy (depicted in red), indicating a significant water content in the surrounding rock. Coupled with the results from TSP analysis (Figure 4a), it is inferred that joint fractures are well-developed in this section, potentially leading to low-flow water bursts. From K6 + 851 m to K6 + 883 m, the coherence energy is weak (appearing in blue), suggesting a low water content in this particular zone. In the interval from K6 + 903 m to K6 + 940 m, the coherence energy is moderate (displayed in pale yellow), implying a moderate water content in the surrounding rock with relatively fewer fissure waters. Nevertheless, the water content is expected to increase correspondingly with an increase in groundwater-surface recharge.

3.2. Deterioration Characteristics of Surrounding Rock Strength in Collapse Zone

To further investigate the physical and mechanical characteristics of the surrounding rock in the collapse zone, detection sections were established at intervals of 1 m within the range of K6 + 831 m to K6 + 840 m. For each detection section, rock samples from the tunnel crown were selected for mineral composition analysis, water damage sensitivity testing, and strength assessment. The class III surrounding rock segment consists of Ordovician biotite quartz schist. The dominant minerals within the collapse zone rock are amphibole, plagioclase, and quartz. The mineral composition proportions are presented in Table 1.

Table 1. Mineral composition and microscopic structure of biotite quartz schist.

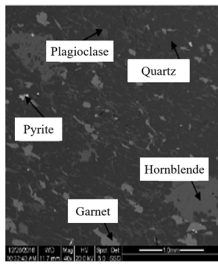
Minerals	Content (%)	Particle Size (mm)	Macrostructure	Microstructure
Hornblende	25	0.50–1.5		
Tremolite	1	0.30–0.50		
Titanite	2	0.05–0.10		
Garnet	3	0.10–0.30		
Plagioclase	37	0.10–0.30		
Quartz	25	0.30–0.50		
Pyrite	5	0.50–1		
Limonite	1	0.05–0.10		
Epidote	1	0.05–0.10		

Figure 5 illustrates the mass loss rate, longitudinal wave velocity, and bearing strength of biotite quartz schist. The impact of groundwater immersion on the physical and mechanical characteristics within the tunnel collapse zone is evident. The bonding material in biotite quartz schist is highly prone to hydrolysis reactions, and the water-rock degradation effect intensifies the deformation and instability of the surrounding rock mass [17]. The mass loss rate escalates with increasing permeating water pressure, with the most substantial increase observed when the pressure rises from 8 MPa to 10 MPa. This indicates that the intensified permeating water pressure accelerates the chemical reaction rate of biotite, increasing the extent of the erosion of pore wall surfaces. The longitudinal wave velocity gradually increases with higher permeating water pressure. This reduction is attributed to the enhanced water erosion capacity under permeating water pressure, leading to increased pore volume and a consequent accelerated attenuation of acoustic energy. Furthermore, biotite quartz schist exhibits pronounced sensitivity to water damage. The uniaxial compressive strength deteriorates noticeably with increasing permeating water pressure. As the permeating water pressure increases from 0 MPa to 6 MPa, the average compressive strength decreases by 63.60%.

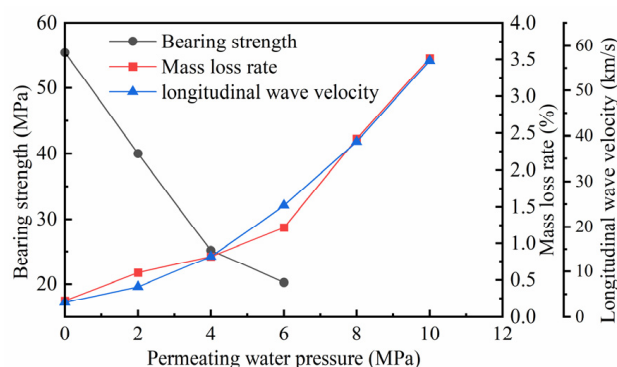


Figure 5. Mass loss rate, longitudinal wave velocity and bearing strength of biotite quartz schist.

In Figure 6, the surrounding rock's bearing strength is depicted at positions A, B, and C in the K6 + 831 m to K6 + 840 m section, with the collapse zone situated at section K6 + 843 m. The average saturated compressive strength of the tested rock samples is

24.80 MPa, which is less than 30 MPa, categorizing them as soft rock. It can be observed that there is a certain level of variability in the strength of the surrounding rock affected by water-rock erosion. As the sampling locations approach the collapse zone, the strength of the tunnel surrounding rocks reduces gradually and logarithmically. This indicates that rock masses closer to the collapse zone have lower bearing strengths.

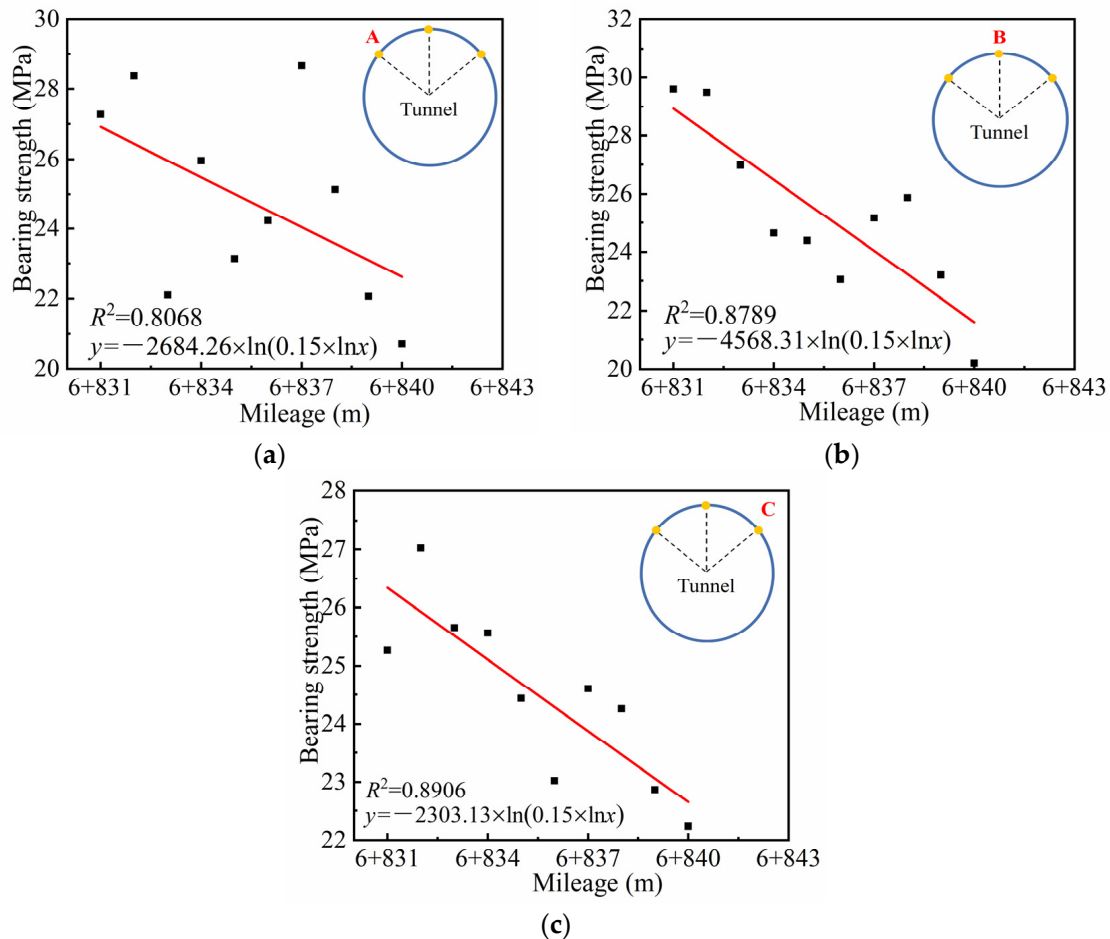


Figure 6. Bearing strength of surrounding rock near the collapse zone: (a) Location A; (b) Location B; and (c) Location C.

3.3. Characteristics of Jointed Rock Mass Inside the Collapse Cavity

Field investigations indicate that the surrounding rock's joint surfaces control the collapse cavity's internal contour. The rock mass behind the collapse cavity's boundary is relatively stable and intact. The surrounding rock in the collapse zone features well-developed joint fissures, and due to structural compression, the rock layers are significantly folded between them. As shown in Figure 7, a considerable amount of rust and chlorination is observed on the fracture surfaces, with mud films adhering to the layer surfaces. The rock mass within the collapse cavity displays a fragmented structure. The cutting action of the cutterhead and the impact of vibrations cause the loosening and dislocation of layers along the joint and fracture surfaces of the sericite schist and biotite quartz schist, ultimately resulting in extensive instability and collapse. Upon clearing the collapsed debris within the cavity, it was discovered that the joint surfaces of the surrounding rock dictate the internal contour of the collapse cavity. The main joint surfaces that constitute the collapse cavity structure include $122^\circ \angle 71.20^\circ$, $108^\circ \angle 81.20^\circ$, and $117^\circ \angle 42.50^\circ$. After clearing the collapsed debris, a stable internal cavity space can be formed.

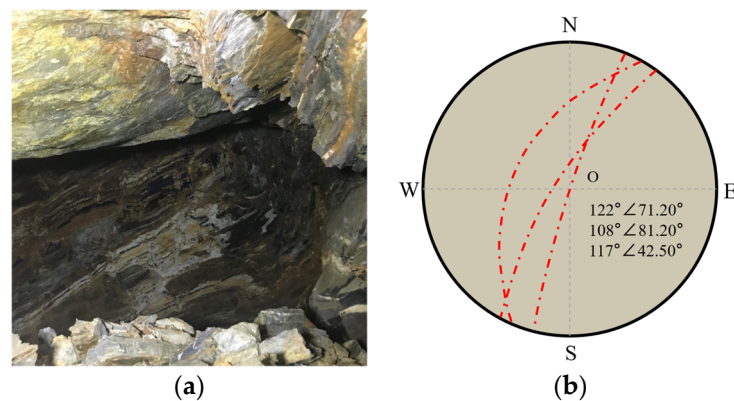


Figure 7. The stable collapse cavity: (a) exposure of surrounding rock and (b) equatorial horizon projection of joint.

4. Collapse Section Treatment Scheme and Feasibility Verification

4.1. Collapse Section Treatment Scheme

Based on the stability characteristics of the collapse cavity after manual debris removal, a preliminary reinforcement scheme has been proposed, including early reinforcement, establishing a protective arch, and the backfilling of the collapse. The site photos of the collapse cavity repair scheme are shown in Figure 8.

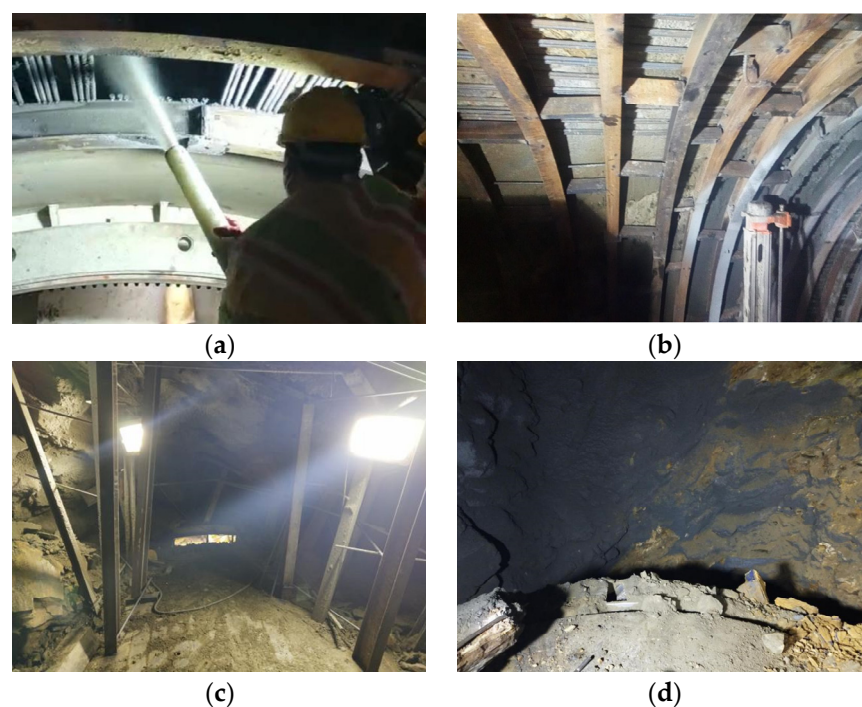


Figure 8. Photos of collapse cavity repair scheme: (a) concrete reinforcement; (b) initial steel arch support; (c) concrete spraying platform for cavity backfilling; and (d) bend covering area and arch protection zone.

Firstly, it is necessary to undertake a preliminary reinforcement of the loose rock mass. The continuous expansion of the collapse zone on the tunnel crown necessitates caution, as the advancing TBM could disturb the surrounding rock, hastening the collapse process. To ensure the safety of personnel and equipment and prevent further expansion of the collapse, the TBM is currently unsuitable for excavation.

After reinforcing the loose rock mass, the TBM will proceed with excavation. The initial step involves spraying concrete on the section where the collapsed height is less

than 2 m within the range of K6 + 838 m to K6 + 840 m, effectively reinforcing the loose rock mass. Enhanced support will be implemented based on the initial support of Class III 1b surrounding rock. HW150 steel arches will be densely placed 6 m behind the shield, with a center-to-center distance of 45 cm (designed spacing of 1.80 m). The arches will be connected using welded 12-channel steel, arranged in a 360° ring at a 1-m spacing, and fully welded at the junctions with H-beams. For areas beyond the reach of the arch installation equipment, arches will be manually erected, followed by the injection of C30 concrete with a reinforcement thickness of 20 cm upon forming the ring. The enhanced arch support system anchor bolts will be promptly installed without causing collapse or sliding.

During the collapse backfilling phase, the restoration process unfolds in a specific sequence. Firstly, square timbers measuring 20 × 20 × 300 cm are laid on the TBM steel shield to establish a concrete spraying platform. Subsequently, I16 I-beams are positioned above the square timbers with a circumferential spacing of 30 cm, connected using welded 12-channel steel. Atop the steel frame, a 0.50 mm steel plate is placed, featuring construction holes measuring 1 × 1 m, forming a closed concrete backfilling surface. This configuration acts as a protective layer on the TBM shield, mitigating the risk of sporadic falling debris causing damage. Within the collapse cavity height range of 2 m (from K6 + 838 m to K6 + 840 m), additional arch supports will be added along the intrados. These arch supports will be closely adhered to the rock surface, with their lower ends firmly welded to the I16 I-beams, forming a stable supporting structure. To prevent the influx of fine sand or cement slurry into the cutter-head area, emergency concrete spraying equipment is employed to spray fine sand within the front 1-m range of the cutterhead. The remaining area is then meticulously filled with C30 concrete, continuing until the fine sand forms a protective buffer layer covering the top of the cutterhead by 10–20 cm.

Moving forward in the restoration sequence, the dense filling process for the collapse cavity begins between K6 + 840 m and K6 + 850 m. C30 concrete is systematically sprayed onto the rock mass, with the effective spray thickness controlled above 10 cm. Above the square timbers, C30 concrete is sprayed with a thickness of 200 cm, ensuring a robust restoration. For every 20 cm thickness of concrete sprayed, a steel mesh (48@200 × 200 mm) is laid. As the concrete thickness reaches 50 cm, I16 I-beams with a longitudinal spacing of 50 cm are set horizontally, reinforcing the structural integrity. Anchoring rods with a diameter of $\varnothing 425$ mm and a length of 2.50 m will be critically installed in the surrounding rock and welded to the I-beams to form a protective arch above the arch supports. Simultaneously, concrete is sprayed within a range of 4 m above the protective arch, extending 7 m towards the cutterhead direction. This establishes a stable support system for the loose rock mass above the tunnel face. The entire restoration process is visually represented in Figure 9.

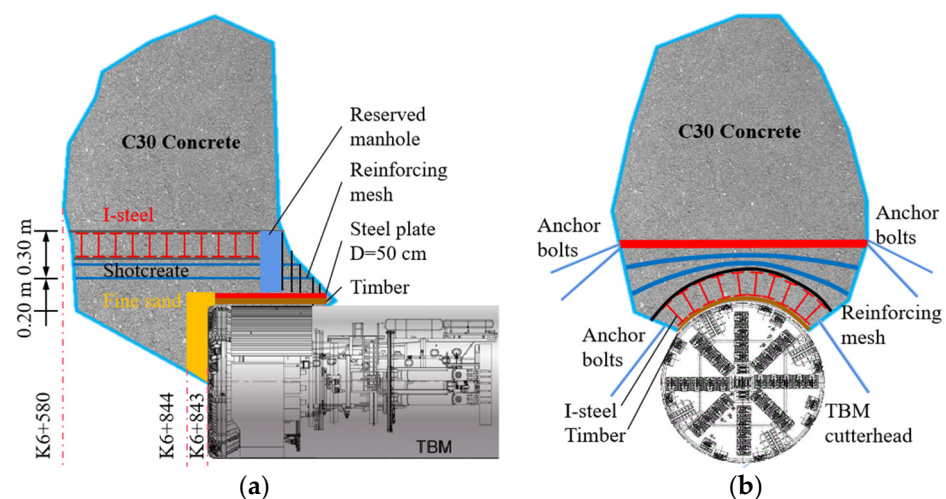


Figure 9. Schematic diagram of the collapse cavity restoration scheme: (a) cutaway-view and (b) front view.

For backfilling of the collapse cavity, C30 concrete will be pumped into the collapse cavity through the reserved manhole pumping pipe, utilizing a concrete delivery pump. The backfilling process will maintain a height above the arch crown, ensuring it does not exceed 1 m at a time until the entire cavity is filled. To alleviate the load on initial and secondary supports, lightweight material with a density of less than 1.5 t/m^3 will be injected into the cavity through the reserved pumping pipe once the backfilling reaches 2 m. Following the filling process, cement mortar will be poured into the gaps to ensure a compact and solid filling.

4.2. Optimization of TBM Excavation Parameters

TBM tunneling is highly complex engineering that requires a dynamic adjustment of excavation parameters based on the surrounding rock conditions. This is especially crucial for collapsed tunnels, as an improper control of the excavation parameters can lead to TBM jamming [24] or even cutterhead damage [25,26]. In this section, we primarily focus on optimizing TBM excavation parameters, considering the collapse section treatment scheme and the characteristics of water-rock dissolution strata. The parameters to be optimized include the total thrust force of the TBM (F_N), the total torque of the cutterhead (F_R), and the frictional mechanical model between the established TBM and the surrounding rock, as illustrated in Figure 10. In the diagram, F_1 represents the thrust force of the cutterhead's front cutters; F_2 represents the friction between the shield structure and the soil layers during forward movement; F_3 represents the friction between the trailing equipment and the inverted structure during traction; F_g represents the thrust force of an individual cutter; F_w represents the pressure exerted by the surrounding rock on the shield; P_0 represents the pressure of the surrounding rock; W_1 is the self-weight of the TBM main body; W_2 is the self-weight of the trailing equipment; and S represents the TBM steel shield's contact area and surrounding rock.

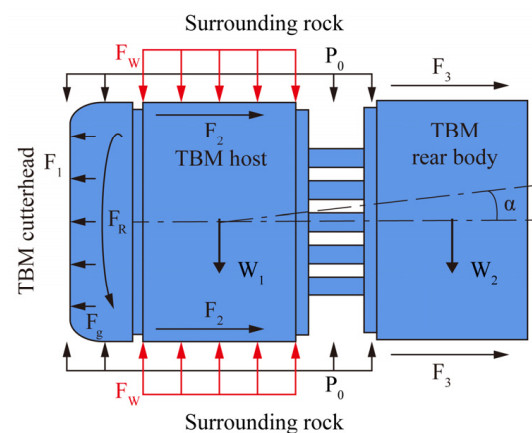


Figure 10. Simple mechanical model of friction between TBM and surrounding rock.

It can be inferred that the total thrust force during TBM excavation is primarily composed of the thrust force of the cutterhead's front cutters F_1 , the friction between the shield structure and the soil layers during forward movement F_2 , and the friction between the trailing equipment and the invert structure during traction F_3 . The total thrust force of the shield must exceed the frictional forces for the TBM to avoid jamming. Based on the Hoek-Brown theory [27] and the relationship between TBM cutterhead and uniaxial compressive strength σ_c , the thrust force of an individual cutter F_g can be expressed as:

$$F_g = 1.50\sigma_c - 1.095 \quad (1)$$

The friction distribution between the shield and surrounding rock is a critical parameter influencing excavation efficiency. It is also a significant factor causing additional stress changes in the surrounding rock of the diversion tunnel during shield tunneling. Based on

the mechanical relationships shown in Figure 10, the frictional force exerted by the shield against the surrounding rock F_2 can be expressed as follows:

$$F_2 = \mu_1(W_1 + F_w) \cos \alpha, \quad (2)$$

$$F_w = S(P_0 - N), \quad (3)$$

$$N = \frac{16P_0m\sigma_c + m^2\sigma_c^2 + 16S\sigma_c^2}{8(8 - m\sigma_c)}, \quad (4)$$

where μ_1 is the coefficient of friction between the steel shield and the rock mass; W_1 is the self-weight of the TBM main body; α is the angle between the tunnel axis and the horizontal line; F_w is the pressure exerted by the surrounding rock on the shield; S represents the contact area between the TBM steel shield and the surrounding rock; P_0 is the pressure of the surrounding rock; N is the reduction in support pressure; and m and s are constants associated with the softness, hardness, and integrity of the rock mass.

If the coefficient of friction between the trailing equipment and the support structure is represented as μ_2 , and the self-weight of the trailing equipment is denoted as W_2 , then the frictional force exerted by the trailing equipment F_3 can be expressed as follows:

$$F_3 = \mu_2W_2 \cos \alpha, \quad (5)$$

Su [28] conducted a study revealing that, for water diversion tunnels, the measured actual torque during TBM construction closely aligns with the calculated results obtained from the Rostami prediction formula [29]. If the TBM cutting coefficient and the cutter-rock interface angle are represented as C and ϕ , respectively, the total rolling torque F_R of the TBM cutter can be expressed as follows:

$$F_R = F_N C = \frac{F_N(1 - \cos \phi)}{\phi - \sin \phi \cos \phi} \quad (6)$$

In this water diversion tunnel project, the TBM cutterhead is equipped with 56 cutters of the 19-inch type. The main TBM machine and the subsequent supporting equipment have self-weights of 7154 kN and 7546 kN, respectively. The tunnel axis is approximately parallel to the horizontal plane. Utilizing the frictional mechanical model between the TBM and the surrounding rock, along with the aforementioned calculation formulas, the total thrust force of the cutterhead F_1 is determined as 2022 kN, the TBM supporting equipment frictional force F_3 is 2461 kN, and the total thrust force F_N is 14,011 kN. The cutter-rock interface angle ϕ of the TBM cutterhead is approximately 15° , leading to a calculated total torque F_R of 1378 kN·m. According to the actual TBM operating conditions, the values of m and s in Equation (4) are taken as 1.213 and 0.00293, respectively. Consequently, the reduction in support pressure N is 1639 kPa.

Based on in-site measurements, the surrounding rock pressure on the tunnel lining P_0 is approximately 1932 kPa, while the pressure exerted by the surrounding rock on the shield body F_w is roughly 16,217 kN. This implies that the frictional force on the shield body F_2 is 9348 kN. Therefore, combining the TBM excavation optimization parameters obtained from Sections 4.1 and 4.2, the total thrust force and the total torque of the cutterhead are determined to be 14,011 kN and 1378 kN·m, respectively. By integrating the measured data and numerical analysis methods, the following evaluation of the re-excavation construction effect and the feasibility verification of disposal measures are conducted.

4.3. Evaluation of Re-Excavation Construction Effect

Re-excavation construction in the collapsed section utilized the initial excavation parameters of the preset TBM, with dynamic adjustments based on on-site rock conditions ensuring safe construction. Figure 11 compares actual total thrust, total torque during TBM excavation in the collapsed section, and optimized parameters.

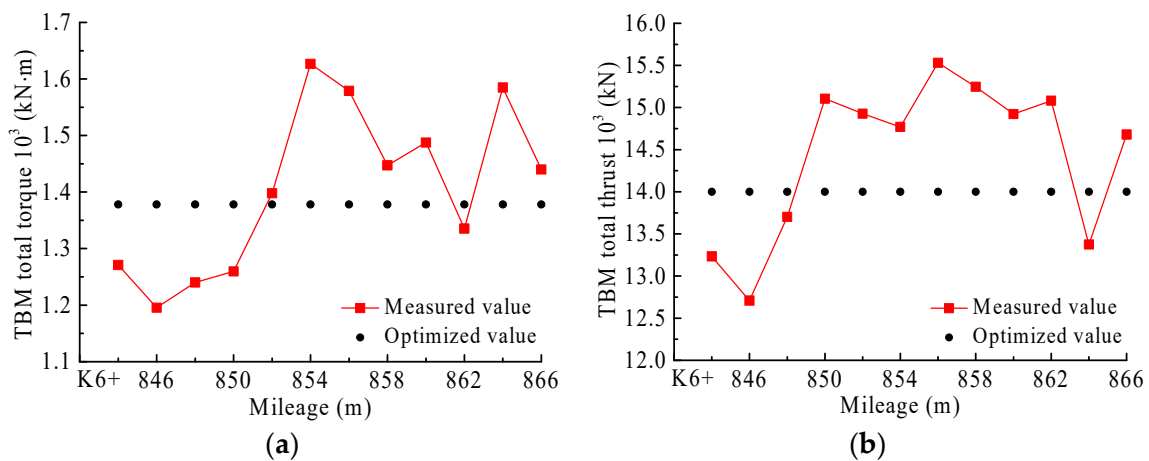


Figure 11. Re-excavation after repairing the collapse cavity: (a) TBM total thrust and (b) TBM total torque.

It is crucial to emphasize that the theoretical model assumes isotropic and uniformly distributed surrounding rock conditions. However, practical engineering scenarios involve variations in rock properties within the rock mass. Therefore, real-time adjustments of TBM excavation parameters are imperative during the construction process, guided by the optimized parameters.

The observation reveals that the adjustment range for TBM excavation thrust and torque stays within 20% of the calculated values, showcasing favorable predictive performance and effective construction guidance. Field monitoring further indicates that the maximum deformation of the surrounding rock stabilizes at approximately 3.58 mm after the collapsed section of the water diversion tunnel. Upon implementing the enhanced reinforcement scheme, the monthly excavation advance rate begins to recover, as depicted in Figure 12. As of the present construction stage, all control indicators remain within the safety range, attesting to the positive re-excavation construction effect and further validating the reliability of the optimized parameters.

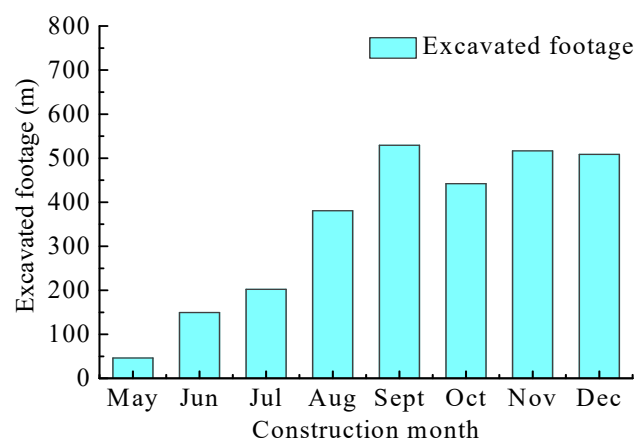


Figure 12. Efficiency of re-excavation after repairing the collapse cavity.

4.4. Feasibility Verification of Treatment Measures

With a significant volume of tunnel collapse and high construction risks, it is essential to validate further the feasibility of the cavity remediation measures within the context of large-scale cavity collapse in the gripper TBM tunnel. To understand the rock deformation, shield pressures, and structural loading of the steel arch, a numerical model was constructed using MIDAS GTS NX analysis software taking into account the actual site conditions. The diversion tunnel is located at a depth of 87.90 m below the ground surface and is considered

a deep-buried tunnel. Disregarding local undulations of the shallow cover soil layer, the established numerical model dimensions are $118 \times 70 \times 127$ m. The outer diameter of the water diversion tunnel is 7.83 m, while the inner diameter is 7 m. The dimensions of the cavity in the water diversion tunnel are $12 \times 10 \times 13.30$ m, as shown in Figure 13.

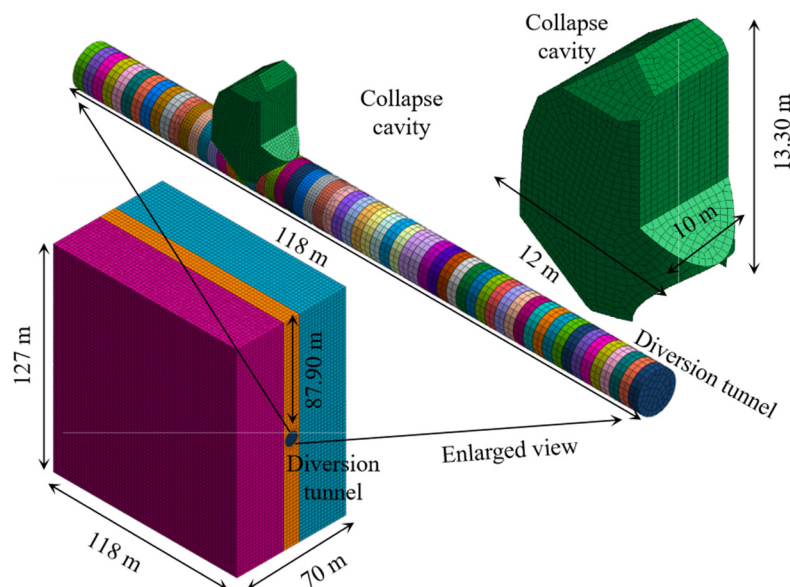


Figure 13. Geometry of the FEA model.

It is important to note that the water diversion tunnel's biotite quartz schist rock mass is simulated using solid elements, applying the Hoek-Brown criterion as the failure criterion for the model. The TBM steel shield and the initial support shotcrete layer are simulated using plate elements, while the steel arch support is simulated using beam elements. The 3D finite element model has a total mesh count of 335,001, with 11,699 mesh elements in the collapsed cavity region and 50,330 mesh elements in the tunnel zone. The model's lateral boundaries are assigned horizontal constraints, the bottom is constrained both vertically and horizontally, and the upper surface is free. Before conducting calculations, an initial stress equilibrium analysis is performed, offering initial stresses to the rock mass and support structures. This establishes a stress field in its natural state with internal forces but no displacement. Subsequently, the stress-strain states of the rock mass and support structures during the TBM excavation process are calculated. Through the integration of on-site surveys, borehole test data, and the proposed cavity treatment plan, the categorization of the surrounding rock has been determined as Grade IV [30]. The physical and mechanical parameters of the numerical model for the water diversion tunnel are presented in Table 2, where γ represents self-unit weight, E is the elastic modulus, ν is the Poisson's ratio, c is the cohesion, and φ is the internal friction angle.

Table 2. Material parameters of 3D finite model.

Material Types	γ (kN/m ³)	E (GPa)	ν	c (kPa)	φ (°)
Surrounding rock (IV)	23	27	0.35	0.7	40
Lightweight concrete backfill	13	25.50	0.30	-	-
Shotcrete (C30)	25	29	0.30	-	-
Steel structure	75	206	0.20	-	-
Steel arch support zone	60	107	0.25	-	-

According to the three-step treatment scheme called "Reinforcement-Backfill-Re-excavation", the FEA model of tunnel excavation simulation was established, as shown in

Figure 14a–c. The flowchart of the repair tunnel cavity sequence was shown in Figure 14d, aligning with the operation procedure in Section 4.1.

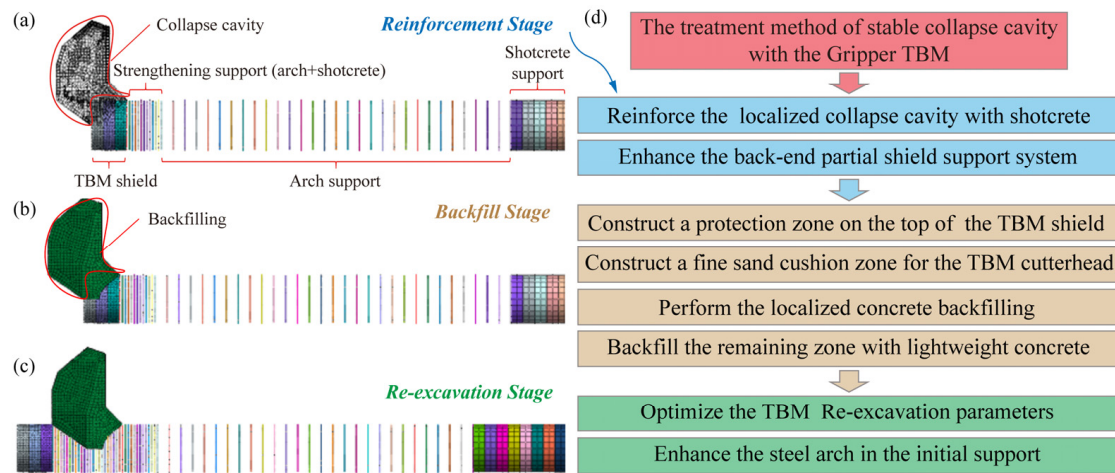


Figure 14. Sequence of repair: (a) reinforcement support; (b) backfill of collapse cavity with multiple steps; (c) re-excitation of TBM; and (d) flow chart of repair sequence.

Figure 15 shows the displacement distribution of surrounding rock in the collapse during TBM tunneling. It is evident that upon the completion of the steel arch reinforcement and initial support shotcrete within the rear 6 m range of the TBM steel shield, a unified support system is formed between the TBM steel shield and the initial support structure. During the reinforcement stage, the maximum displacement of the collapsed rock mass is 3.58 mm, representing the highest value throughout the entire construction process of the treatment plan, as shown in Figure 15a. Following the completion of the initial support, the backfilling of the collapsed cavity effectively mitigates the deformation of the collapsed rock mass, resulting in a maximum deformation displacement of 3.15 mm. This represents a reduction of 12.01% compared to the reinforcement stage. As depicted in Figure 15c, with the backfilling of the collapsed cavity and the ongoing tunnel excavation, the distribution of rock mass deformation displacement in the surrounding area reaches a relatively stable state, displaying consistent trends in the evolution of displacement distribution clouds. In comparison to the backfilling stage, the maximum deformation displacement during the re-excitation stage is 3.10 mm, representing a marginal reduction of 1.59%. It is evident that the displacement of the collapsed rock mass gradually converges during the TBM excavation process. The reinforcement of the collapsed rock mass and the backfilling measures within the collapsed cavity significantly control rock mass deformation, ensuring the safe construction of the TBM.

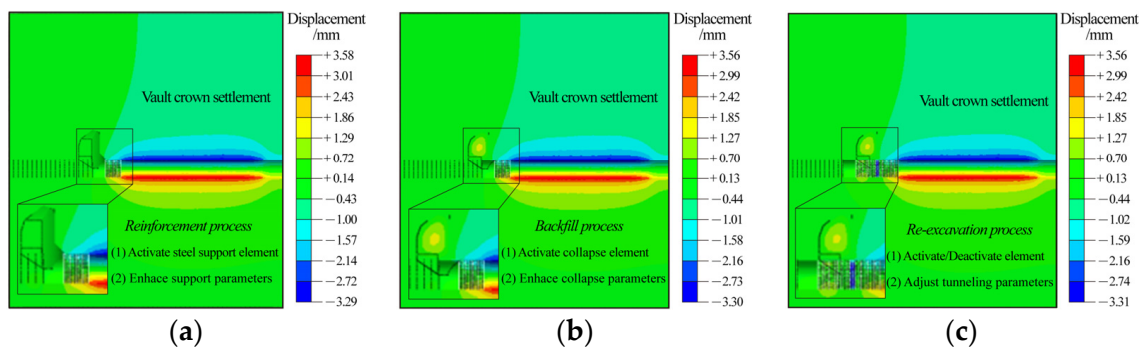


Figure 15. Displacement distribution of surrounding rock in the collapse during TBM tunneling: (a) reinforcement stage, (b) backfill stage, and (c) re-excitation stage.

Figure 16 illustrates the stress distribution on the steel shield during the TBM excavation process. Before the collapse, the TBM steel shield served as the primary load-bearing structure responsible for managing concentrated stresses in the collapsed zone. The distribution and magnitude of compressive stress are notably influenced by the collapsed cavity. Owing to the abrupt change in structural stiffness between the TBM steel shield and the densified segment of the arch, a concentrated compressive stress region forms at the rear of the TBM shield. The stress at the top of the shield is significantly higher than at the bottom, peaking at 6.96 MPa, as illustrated in Figure 16a. The lightweight concrete used for cavity backfilling increases the upper load of the steel shield and support system. The filled concrete restores the arch defect caused by the cavity collapse, creating an arch effect within the tunnel and optimizing the stress distribution of the rock mass. In comparison to the reinforcement stage, the stress distribution of the shield structure during the cavity backfilling stage does not change significantly. The concentrated stress region at the top of the shield reduces, and the maximum compressive stress decreases from 6.96 MPa to 6.61 Mpa, as illustrated in Figure 16b. After the TBM excavates through the collapsed section, the shield structure enters the intact rock mass, and the concentrated stress in the collapsed zone is borne by the arch structure of the densified segment. The stress cloud maps show that the concentration of stress at the top of the TBM steel shield disappears, and the tensile stress significantly decreases, with the maximum compressive stress dropping from 6.61 Mpa to 3.67 Mpa. As the tunneling progresses, the maximum compressive stress of the shield structure shifts from the top to the bottom of the shield, with the bottom bearing 1.38 times the stress of the top, as shown in Figure 16c. Based on the stress characteristics of the TBM steel shield in three stages, it is evident that the peak stresses in the shield structure are below the material strength. This indicates that the cavity backfilling measures effectively control deformation, thus preventing TBM jamming.

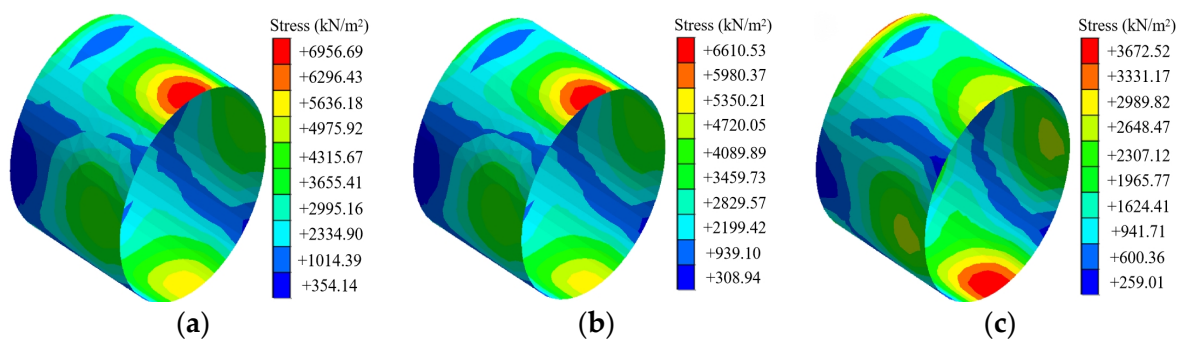


Figure 16. Stress distribution of TBM shield during TBM tunneling: (a) reinforcement stage, (b) backfill stage, and (c) re-excavation stage.

Figure 17 presents the stress distribution cloud map of the densified segment arch of the TBM. Prior to entering the collapsed zone, the densified segment arch serves as a supporting structure, shouldering a fraction of the concentrated stress in that area. Stress distribution within the arch varies from -1.28 MPa to -0.092 MPa (with “-” indicating tensile stress). Notably, tensile stress is most prominent at the arch’s crown, intensifying as the arch nears the collapsed cavity. The highest compressive stress is observed at the crown of the first arch behind the TBM shield. Following cavity backfilling, rock mass stress distribution is optimized, leading to a narrowed stress range for the arch, now spanning from -0.43 MPa to 0.073 MPa. The peak tensile stress in the steel arch remains at the crown of the first arch behind the TBM shield. As the TBM progresses, distancing itself from the collapsed zone, the densified segment arch takes on the primary load-bearing role for concentrated stress in that area. The stress distribution range widens within the collapsed zone, ranging from -2.22 MPa to -0.29 MPa, with the maximum compressive stress persisting at the arch’s crown. Notably, the peak stress location shifts to the boundary of the collapsed zone. During the cavity treatment plan’s construction phase,

rock mass displacement and deformation stabilize, with both tensile and compressive stresses in the TBM steel shield and initial support steel arch staying below material strength. Implementing the proposed treatment plan for the open-type TBM cavity collapse ensures stable rock mass conditions and the safety of the support structure.

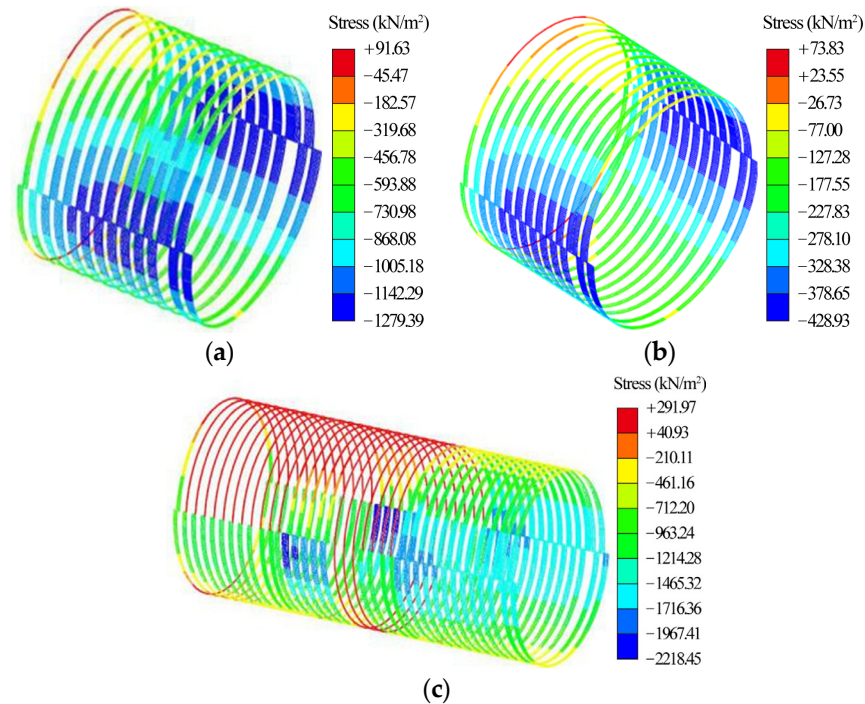


Figure 17. Stress distribution of arch during TBM tunneling: (a) reinforcement stage, (b) backfill stage, and (c) re-excavation stage.

5. Conclusions

The large-scale collapse of the gripper TBM during the excavation of the diversion tunnel was studied. Various methods, such as TSP seismic wave detection, CFC advanced water detection, the laboratory point load test, and the packer permeability test, were used to analyze the causes of the large-scale collapse comprehensively. A TBM collapse disposal technique was proposed, thus involving the construction of a protective shell inside the cavity of the arch. The following conclusions were drawn:

- (1) The TSP seismic wave detection results indicate that the surrounding rock near the collapse cavity is characterized by joint fissures and fold development, with the rock mass being fragmented and of lower strength. CFC advanced water detection results show that the average dielectric constant of the surrounding rock in the collapse cavity is 2.841, with only a tiny number of water-filled fissures present in the rock mass. Point load test results indicate a logarithmic decrease in the uniaxial compressive strength of the rock as the sampling location approaches the collapse area. Packer permeability tests uncover notable water-softening characteristics in the biotite-quartz schist. The collapse zone experiences extensive instability and collapse due to joint fissures, rock fragmentation, weak interlayer bonding, and a limited amount of groundwater. These factors, compounded by the cutting action of the cutterhead and vibrations, constitute the fundamental reasons behind this issue.
- (2) A three-step treatment scheme of “Reinforcement-Backfill-Re-excavation” is proposed in view of the characteristics of forming a stable collapse cavity in the collapse zone. The reinforcement stage adopts measures to reinforce the cavity rock and strengthen the support structure based on numerical simulation and calculations, forming a support system consisting of both the TBM shield and the dense steel arch. The deformation of the surrounding rock reaches a maximum of 3.58 mm during the

implementation of the treatment scheme, which is the largest value observed during the construction. The surrounding rock has no sudden deformation in the backfill and re-excavation stage, and the risk of jamming is minimized. The most critical arch position shifts from the first arch behind the TBM shield to the boundary of the collapse zone with the implementation of the treatment scheme, and the peak stresses in the steel arches occur at the arch crowns.

- (3) The construction steps of the stable collapse repair scheme include collapse cavity reinforcement, enhanced support, construction platform setup, coving construction for the cutterhead, the backfilling of the collapse, an adjustment of excavation parameters, and a gradual reinforcement of the support. After verification through calculations, the scheme has been successfully applied to treat the collapse zone. It maximizes the use of stable cavity space as a construction platform, reducing the treatment time from 28 days to 13 days. This significantly enhances construction efficiency for the cutterhead protective layer and collapse backfilling. The scheme serves as a valuable reference for addressing collapses with a stable cavity space.

Funding: This research was funded by the Tunnel and Underground Engineering New Technology and Application Innovation Team of Shaanxi Province Science and Technology Innovation Team Project (No. 2020TD-005).

Data Availability Statement: All data that support the findings of this study are available from the corresponding author upon reasonable request.

Conflicts of Interest: Author Tengtian Yang was employed by the company China Railway Construction Bridge Engineering Bureau Group Co., Ltd. The author declares that the research was conducted in the absence of any commercial or financial relationships that could be construed as a potential conflict of interest.

Appendix A. Tunnel Seismic Prediction (TSP) and Complex Frequency Conductivity (CFC)

Appendix A.1. Tunnel Seismic Prediction (TSP)

Tunnel Seismic Prediction (TSP) stands as a cutting-edge technique employed for subsurface exploration. Its fundamental principle involves generating seismic waves within underground structures and subsequently measuring and analyzing the propagation characteristics of these waves to extract geological and structural information. By detecting reflections and refractions at different subsurface layers, TSP provides crucial insights into the nature of underground structures, soil properties, and potential hazards.

Appendix A.2. Complex Frequency Conductivity (CFC)

Complex Frequency Conductivity (CFC) emerges as a novel electromagnetic wave exploration technique, abbreviated as CFC. This method relies on measuring the response of subsurface media to electromagnetic waves and analyzing variations in complex frequency conductivity to infer properties of the underground medium. CFC finds widespread applications in water resource exploration and underground water level monitoring.

References

1. Zheng, Y.L.; Zhang, Q.B.; Zhao, J. Challenges and opportunities of using tunnel boring machines in mining. *Tunn. Undergr. Space Technol.* **2016**, *57*, 287–299. [[CrossRef](#)]
2. Fan, S.Y.; Song, Z.P.; Zhang, Y.W.; Liu, N.F. Case study of the effect of rainfall infiltration on a tunnel underlying the roadbed slope with weak inter-layer. *KSCE J. Civ. Eng.* **2020**, *24*, 1607–1619. [[CrossRef](#)]
3. Fan, S.Y.; Song, Z.P.; Xu, T.; Wang, K.M.; Zhang, Y.W. Tunnel deformation and stress response under the bilateral foundation pit construction—A case study. *Arch. Civ. Mech. Eng.* **2021**, *109*, 109. [[CrossRef](#)]
4. Dong, L.; Song, D.; Liu, G. Seismic wave propagation characteristics and their effects on the dynamic response of layered rock sites. *Appl. Sci.* **2022**, *12*, 758. [[CrossRef](#)]
5. Tian, X.X.; Song, Z.P.; Zhang, Y.W. Monitoring and reinforcement of landslide induced by tunnel excavation: A case study from Ximaixi tunnel. *Tunn. Undergr. Space Technol.* **2020**, *110*, 103796. [[CrossRef](#)]

6. Tian, X.X.; Song, Z.P.; Wang, H.Z.; Zhang, Y.W.; Wang, J.B. Evolution characteristics of the surrounding rock pressure and construction techniques: A case study from Taoshuping tunnel. *Tunn. Undergr. Space Technol.* **2022**, *125*, 104522. [[CrossRef](#)]
7. Zhang, Y.; Wang, J.; Liu, F.; Xia, H. Mechanism and Sensitivity Analysis of Collapse in Large Section Mountain Neighborhood Tunnels. *Front. Earth Sci.* **2022**, *10*, 904655. [[CrossRef](#)]
8. Zhao, M.; Cheng, Y.; Song, Z.; Wang, T.; Zhang, Y.; Gong, Y.; Song, Y. Stability Analysis of TBM Tunnel Undercrossing Existing High-Speed Railway Tunnel: A Case Study from Yangtaishan Tunnel of Shenzhen Metro Line 6. *Adv. Civ. Eng.* **2021**, *2021*, 6674862. [[CrossRef](#)]
9. Bayati, M.; Hamidi, J.K. A case study on TBM tunnelling in fault zones and lessons learned from ground improvement. *Tunn. Undergr. Space Technol.* **2017**, *63*, 162–170. [[CrossRef](#)]
10. Han, X.; Liang, X.; Ye, F.; Wang, X.; Chen, Z. Statistics and construction methods for deep TBM tunnels with high geostress: A case study of Qinling Tunnel in Hanjiang-Weihe River Diversion Project. *Eng. Fail. Anal.* **2022**, *138*, 106301. [[CrossRef](#)]
11. Acun, S.; Bilgin, N.; Erboylu, U. Contribution on the understanding of EPB-TBM drives in complex geologic structures. *Tunn. Undergr. Space Technol.* **2021**, *07*, 103646. [[CrossRef](#)]
12. Koizumi, Y.; Inaba, T.; Yamamoto, T. Theoretical analysis and seismic investigation for TBM jamming in squeezing fissile slate. *Tunn. Undergr. Space Technol.* **2016**, *57*, 284–286. [[CrossRef](#)]
13. Xu, Z.H.; Wang, W.Y.; Lin, P.; Nie, L.C.; Wu, J.; Li, Z.M. Hard-rock TBM jamming subject to adverse geological conditions: Influencing factor, hazard mode and a case study of Gaoligongshan Tunnel. *Tunn. Undergr. Space Technol.* **2021**, *108*, 103683. [[CrossRef](#)]
14. Abdollahi, M.S.; Najafi, M.; Bafghi, A.Y.; Marji, M.F. A 3D numerical model to determine suitable reinforcement strategies for passing TBM through a fault zone, a case study: Safaroud water transmission tunnel, Iran. *Tunn. Undergr. Space Technol.* **2019**, *88*, 186–199. [[CrossRef](#)]
15. Zhang, J.; Li, S.; Zhang, Q.; Zhang, X.; Li, P.; Wang, D.; Weng, X. Mud inrush flow mechanisms: A case study in a water-rich fault tunnel. *Bull. Eng. Geol. Environ.* **2019**, *78*, 6267–6283. [[CrossRef](#)]
16. Sun, B.; Yang, S. An improved 3D finite difference model for simulation of double shield TBM tunnelling in heavily jointed rock masses: The DXL tunnel case. *Rock Mech. Rock Eng.* **2019**, *52*, 2481–2488. [[CrossRef](#)]
17. Song, Z.P.; Song, W.X.; Cheng, Y.; Yang, T.T.; Wang, T.; Wang, K.S. Investigation on strain characteristics and fatigue constitutive model of limestone under osmotic pressure and cyclic disturbance coupling. *KSCE J. Civ. Eng.* **2021**, *26*, 1416–1429. [[CrossRef](#)]
18. Cheng, Y.; Song, Z.P.; Chang, X.X.; Wang, T. Energy evolution principles of shock-wave in sandstone under unloading stress. *KSCE J. Civ. Eng.* **2020**, *24*, 2912–2922. [[CrossRef](#)]
19. Yang, T.T.; Li, H.; Zhou, G.N.; Guo, W. Pregrouting reinforcement technology of open TBM in soft stratum. *Tunn. Constr.* **2021**, *41*, 858–864. (In Chinese)
20. Song, Z.P.; Cheng, Y.; Zhang, Z.K.; Yang, T.T. Tunnelling performance prediction of cantilever boring machine in sedimentary hard-rock tunnel using deep belief network. *J. Mt. Sci.* **2023**, *20*, 2029–2040. [[CrossRef](#)]
21. Li, S.; Nie, L.; Liu, B. The practice of forward prospecting of adverse geology applied to hard rock TBM tunnel construction: The case of the Songhua River water conveyance project in the middle of Jilin Province. *Engineering* **2018**, *4*, 131–137. [[CrossRef](#)]
22. Cheng, Y.; Song, Z.P.; Yang, T.T.; Han, J.J.; Wang, B.W.; Zhang, Z.K. Investigating the aging damage evolution characteristics of layered hard sandstone using digital image correlation. *Constr. Build. Mater.* **2022**, *353*, 128838. [[CrossRef](#)]
23. Jiang, H.; Hou, J.; Lu, P. Application of TST and CFC integrated technology in KS tunnel advanced geology prediction. *Mod. Tunn. Tech.* **2018**, *S2*, 758–763.
24. Lin, P.; Yu, T.; Xu, Z.; Shao, R.; Wang, W. Geochemical, mineralogical, and microstructural characteristics of fault rocks and their impact on TBM jamming: A case study. *Bull. Eng. Geol. Environ.* **2022**, *81*, 64. [[CrossRef](#)]
25. Li, X.; Wu, J.Q.; Huo, P. Prediction Model for the Teeth Hob Cutter of Tunnel Boring Machines in High-content Quartzite Strata. *KSCE J. Civ. Eng.* **2023**, *27*, 371–383. [[CrossRef](#)]
26. Li, X.; Wu, J.Q.; Huo, P.; Gong, Z.B.; Su, P.D. Analysis of the Influencing Factors and Prediction of the Service Life of a Shield Machine Cutter: A Case Study of the Guangfo East Ring Tunnel in Guangdong, China. *Transp. Res. Rec.* **2023**, *2677*, 639–651. [[CrossRef](#)]
27. Hoek, E.; Kaiser, P.K.; Bawden, W.F. *Support of Underground Excavations in Hard Rock*; CRC Press: Boca Raton, FL, USA, 2000.
28. Su, H. Study on Surrounding Rock Stability of Deep Tunnel by Double-Shield TBM Excavation. Doctoral Thesis, Southwest Jiaotong University, Chengdu, China, 2009; pp. 12–31.
29. Rostami, J. Hard rock TBM cutterhead modeling for design and performance prediction. *Geomech. Tunnelbau* **2008**, *1*, 18–28. [[CrossRef](#)]
30. Fu, X.L.; Wu, M.Z.; Zhang, L.M. Probabilistic Life Prediction of Tunnel Boring Machine under Wearing Conditions with Incomplete Information. *Buildings* **2022**, *12*, 1959. [[CrossRef](#)]

Disclaimer/Publisher’s Note: The statements, opinions and data contained in all publications are solely those of the individual author(s) and contributor(s) and not of MDPI and/or the editor(s). MDPI and/or the editor(s) disclaim responsibility for any injury to people or property resulting from any ideas, methods, instructions or products referred to in the content.